Showcasing an anomalous layer-dependent band gap of two-dimensional Bi_2OS_2 caused by surface electronic states, predicted by Prof. Yunfei Chen and Prof. Jinlan Wang at Southeast University in China.

Bi_2OS_2: a direct-gap two-dimensional semiconductor with high carrier mobility and surface electron states

Bi_2OS_2 nanosheets exhibit tunable anomalous layer-dependent band gaps, which is a result of the synergetic effect of the quantum confinement and surface electron states. Meanwhile, their ultra-high electron mobility and excellent stability are also highly desirable for optoelectronic applications.

As featured in:

See Yunfei Chen, Jinlan Wang *et al.*, *Mater. Horiz.*, 2018, **5**, 1058.

ROYAL SOCIETY
OF **CHEMISTRY**

rsc.li/materials-horizons

Registered charity number: 207890

Materials Horizons

ROYAL SOCIETY OF CHEMISTRY

COMMUNICATION

View Article Online
View Journal | View Issue

Cite this: *Mater. Horiz.*, 2018, 5, 1058

Received 21st August 2018, Accepted 13th September 2018

DOI: 10.1039/c8mh01001c

rsc.li/materials-horizons

Published on 13 září 2018. Downloaded by Fail Open on 07.05.2025 10:35:25.

Bi_2OS_2: a direct-gap two-dimensional semiconductor with high carrier mobility and surface electron states†

Xiwen Zhang,‡[a] Bing Wang,‡[b] Xianghong Niu,[c] Yunhai Li,[b] Yunfei Chen*[d] and Jinlan Wang *[b]

Two-dimensional (2D) semiconductors with desirable band gaps and high carrier mobility are highly sought after for future application in nanoelectronics. Herein, by means of first-principles calculations, we predict that a new 2D material, namely a Bi_2OS_2 nanosheet, possesses not only a tunable direct band gap, but also ultra-high electron mobility (up to 26 570 cm^2 V^{-1} s^{-1}). More interestingly, an anomalous layer-dependent band gap is revealed, derived from the synergetic effect of the quantum confinement and intrinsic surface electron states. 2D Bi_2OS_2 also exhibits excellent absorption over the entire solar spectrum and the absorption coefficient is comparable to that of inorganic–organic hybrid perovskite solar cells. Moreover, the Bi_2OS_2 monolayer maintains good structural integrity up to 1000 K and has a relatively small exfoliation energy from its layered bulk. The excellent electronic and optical properties, together with high stability and great experimental possibility, render 2D Bi_2OS_2 a promising material for future nanoelectronic and optoelectronic applications.

Conceptual insights

For the application of two-dimensional (2D) materials in digital electronics and optoelectronics, a tunable and sizable band gap and high mobility are essential. The tunable band gap usually decreases with an increase in the number of layers and approaches the bulk limitation. In this article, we predict a new 2D layered Bi_2OS_2 with an anomalous layer-dependent band gap, which first decreases and reaches a minimum value at the 8th layer and increases afterward with the increase of stacking layers. The detailed studies indicate that this kind of anomaly, reported for the first time, is a result of the synergetic effect of the quantum confinement and intrinsic surface electron states. The new concept of electronic structures affected by the synergism of the quantum confinement effect and intrinsic surface electron states opens up a new understanding of 2D BiS_2-based layered semiconductors, and this kind of anomaly reduces the challenge to create ultra-thin semiconductors with specific absorption spectra suitable for photo-detection. Meanwhile, 2D layered Bi_2OS_2 possesses a direct and moderate band gap, ultra-high electron mobility, and good stability in one, which also shows great potential applications in electronic and optoelectronic fields.

Introduction

The family of two-dimensional (2D) nanomaterials has triggered a surge of research interest due to their desirable electronic and optical properties.[1–3] Nevertheless, drawbacks exist in these 2D materials, which make it impossible for them to meet all practical demands. For example, the gapless nature of graphene makes it unsuitable for effectively switching current on and off in digital transistors.[4] The relatively low carrier mobility of transition metal dichalcogenides limits their applications in high-performance electronic devices.[5,6] The poor stability of black phosphorus leads to rapid performance degradation when exposed to air.[7,8] Hence, it is still desirable to discover new 2D materials that simultaneously possess a moderate band gap, high mobility, and good stability.

In the past few years, much attention has been paid to a series of 2D Bi-based semiconductors, such as BiOX (X = Cl, Br and I) nanosheets, Bi_2Y_3 (Y = O and S) nanosheets, and so on.[9–12] The well-dispersed Bi 6s orbital increases carrier mobility, making these materials promising candidates when compared to other 2D metal oxide semiconductors.[13,14] Unfortunately, BiOBr and BiOI nanosheets suffer from serious photo-decomposition under light illumination.[15,16] Bi_2O_3 and Bi_2S_3 nanosheets have rather large light absorption edges (2.8 eV for Bi_2O_3; 1.9 eV for Bi_2S_3) which allows efficient collection of solar emission.[12,17,18] Partial replacement of X atoms with S atoms in BiOX or mixing O atoms with S atoms in Bi_2Y_3 can form a van der Waals (vdWs) layered

[a] *School of Mechanism Engineering & School of Physics, Southeast University, Nanjing 211189, China*
[b] *School of Physics, Southeast University, Nanjing 211189, China. E-mail: jlwang@seu.edu.cn*
[c] *School of Science, Nanjing University of Posts and Telecommunications, Nanjing 210046, China*
[d] *School of Mechanism Engineering, Southeast University, Nanjing 211189, China. E-mail: yunfeichen@seu.edu.cn*

† Electronic supplementary information (ESI) available. See DOI: 10.1039/c8mh01001c
‡ These authors contributed equally to this work.

 This journal is © The Royal Society of Chemistry 2018

Published on 13 září 2018. Downloaded by Fail Open on 07.05.2025 10:35:25.

material, Bi_2OS_2. In fact, vdW layered Bi_2OS_2 bulk has been successfully synthesized, and exhibits direct optical transitions and good electronic properties.[19] The crystal structure of the layered compound Bi_2OS_2 is similar to that of BiOX. Two opposite $[BiS_2]^-$ layers separate two $[Bi_2O_2]^{2+}$ layers in Bi_2OS_2, different from the two columns of X^- anions in BiOX. As a result, the presence of $[BiS_2]^-$ layers is expected to stabilize the material under sunlight irradiation, and meanwhile the mixing of O atoms and S atoms would narrow the band gap of Bi_2Y_3. Therefore, discrete 2D Bi_2OS_2 nanosheets might be good candidates for high-speed micro-/nano-optoelectronic devices.

In this work, we employ first-principles methods to investigate the dynamical and chemical stability, experimental feasibility, and electronic and optical properties of monolayer and few layered Bi_2OS_2, which are possibly exfoliated from the layered solid. It is revealed that the Bi_2OS_2 monolayer possesses a small exfoliation energy (0.47 J m^{-2}) from its bulk counterpart and maintains good structural stability up to 1000 K. Meanwhile, 2D Bi_2OS_2 exhibits a moderate direct band gap, high carrier mobility and strong light absorption in the infrared, visible and UV regions. More notably, the band gap of 2D layered Bi_2OS_2 shows an anomalous layer-dependent relationship, *i.e.*, the band gap first declines from 0.97 eV (monolayer) to the minimum value of 0.59 eV (8-layer), and then increases with the increase of stacking layers. The anomaly arises from the synergism of the quantum confinement (QC) effect and intrinsic surface electron states (SESs).

Results and discussion

Structure and stability of the Bi_2OS_2 monolayer

The bulk Bi_2OS_2 has a stable layered structure with the tetragonal *P*4/*nmm* space group (Fig. S1, ESI†), and can be viewed as stacked parallel sheets, which interact with one another through vdW interactions. Each sheet can be viewed as a three-layer stacking of BiO and BiS_2, wherein the BiO layer is sandwiched by BiS_2 layers (Fig. 1a). Mechanical cleavage and liquid phase exfoliation[20,21] have been widely used to produce single and few-layer flakes from the layered bulk. To assess the exfoliation feasibility of the Bi_2OS_2 monolayer, we calculated the cleavage energy by introducing a fracture in the bulk Bi_2OS_2 (Fig. 1b). The calculated cleavage energy of 0.47 J m^{-2} is comparable to that of graphite, which is about 0.33 J m^{-2} from our calculation or 0.36 J m^{-2} from experiment.[22] This result suggests that the exfoliation of a Bi_2OS_2 monolayer from its solid should be feasible experimentally. Furthermore, the thermal stability of the Bi_2OS_2 monolayer has been examined by performing *ab initio* molecular dynamics (AIMD) simulations at different temperatures (Fig. 1c and Fig. S2, ESI†). This shows that the Bi_2OS_2 monolayer retains its structure well up to 1000 K (see Fig. 1c), indicative of its high thermal stability. The phonon dispersion curves of the Bi_2OS_2 monolayer contain only real modes (Fig. 1d), suggesting its kinetic stability as well. Moreover, higher chemical stability is expected for the Bi_2OS_2 monolayer, as its work function of 5.27 eV (Fig. 1e) is substantially higher than that of graphene (4.46 eV)[23] and phosphorene (4.25 eV).[24]

Electronic properties of monolayer and few-layer Bi_2OS_2

Next, we investigated the electronic structures of monolayer and few-layer Bi_2OS_2. As shown in Fig. 2a and Fig. S3 (ESI†), both monolayer and few-layer Bi_2OS_2 exhibit direct semiconducting behavior with the conduction band minimums (CBMs) and the valence band maximums (VBMs) located at the *X* point. The band gap of the Bi_2OS_2 monolayer is about

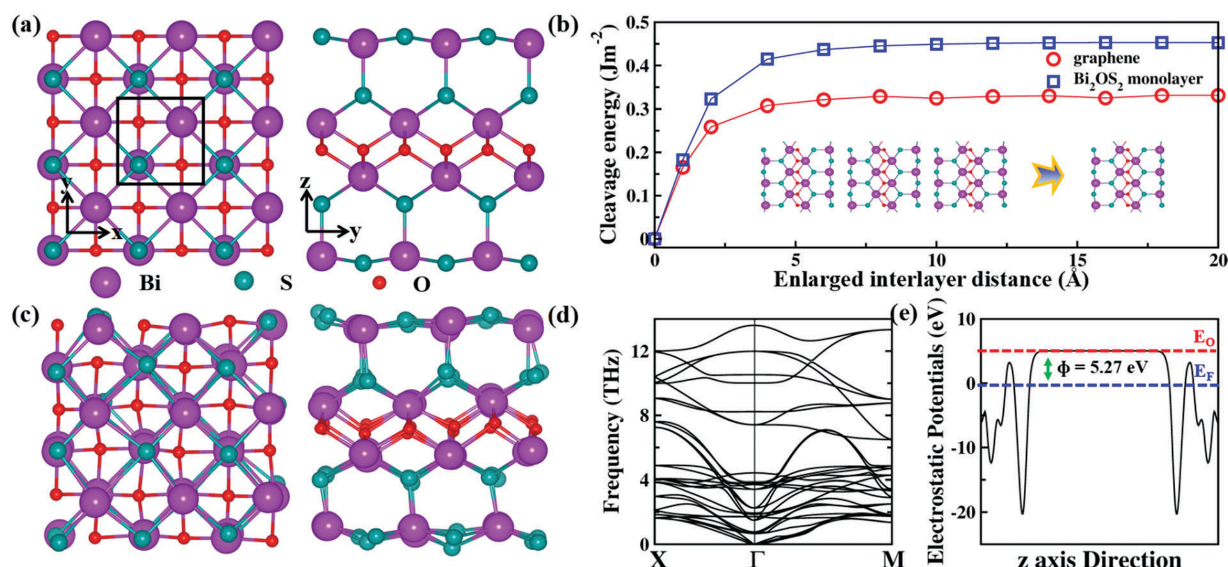

Fig. 1 (a) Structure (top and side views) of the Bi_2OS_2 monolayer. The tetragonal unit cell is enclosed in the black solid line. (b) Cleavage energy *versus* the separation distance for planar fracture within the bulk Bi_2OS_2. The cleavage energy for graphite is also plotted for comparison. (c) Snapshots of atomic configurations at a temperature of 1000 K at the end of 5 ps, (d) phonon spectrum, and (e) electrostatic potentials of the Bi_2OS_2 monolayer. The red and blue dashed lines represent the vacuum level (E_O) and the Fermi level (E_F), respectively. Φ is the work function.

Published on 13 září 2018. Downloaded by Fail Open on 07.05.2025 10:35:25.

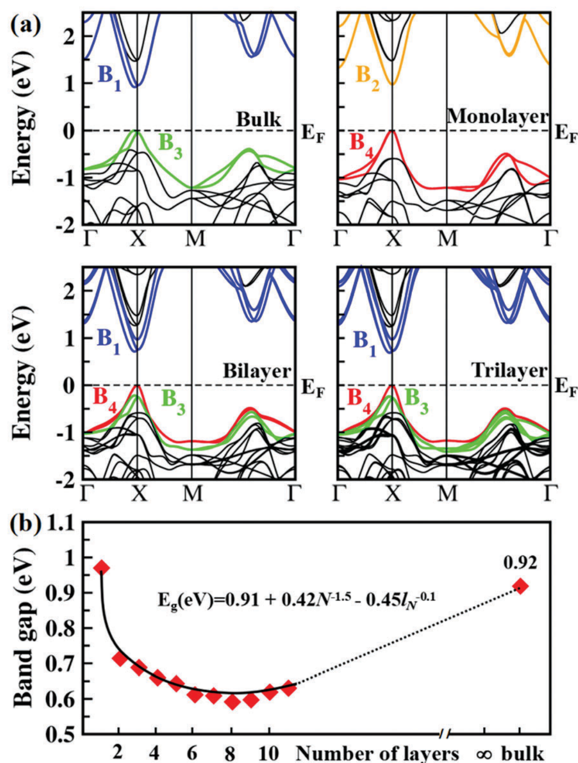

Fig. 2 (a) Calculated band structures of bulk, monolayer, and few-layer Bi_2OS_2. (b) The band gaps of bulk and 2D Bi_2OS_2. l_N is the distance between the two outermost layers of 2D Bi_2OS_2 and depends linearly on the number of layers (N), as shown in Fig. S4 (ESI†).

0.97 eV, which is slightly larger than that of the bulk (0.92 eV). Nevertheless, few-layered Bi_2OS_2 has a smaller band gap than that of the bulk, which is different from most cases, such as group-VA semiconductors, transition metal dichalcogenides (TMDs), and other layered Bi-based semiconductors.[25–29] More surprisingly, we observe an anomalous layer-dependent behavior in the band gap of 2D Bi_2OS_2. As shown in Fig. 2b, the band gap first declines from 0.97 eV (monolayer) to the minimum value of 0.59 eV (8-layer), and then approaches the bulk limit (0.92 eV) with the increase of the stacking layers. These anomalies in the band gap cannot be well explained by the QC effect alone, which normally would enlarge the gap and make the gap follow the $B + AN^{-\alpha}$ relationship[28,29] (N is the layer number). In fact, we note that the band structures are also changed when the bulk Bi_2OS_2 is exfoliated into a monolayer and few-layers. Four sets of bands near the Fermi level (Fig. 2a) of Bi_2OS_2 are highlighted in blue (B_1), orange (B_2), green (B_3) and red (B_4), respectively. Very interestingly, B_3 and B_4 bands exist alone in the bulk and monolayer Bi_2OS_2, respectively, while they both appear in the few-layer Bi_2OS_2 (see Fig. 2a and Fig. S3, ESI†). The conjunction of the unique band structure and the anomalous behavior in the band gap leads to a proper deduction that the anomaly is closely related to the appearance of B_4 bands in 2D Bi_2OS_2.

It is well-known that the band structure largely depends on the charge distribution of atoms in the lattices. To deeply understand the unique band structure near the Fermi level, we calculated the band decomposed charge density of the B_1, B_2, B_3, and B_4 bands of the bulk, monolayer, and few-layer Bi_2OS_2, as appropriate. As clearly shown in Fig. S5 (ESI†), the charge densities of the B_1 and B_2 bands are distributed around the bismuth, sulfur and oxygen atoms inside the crystal, suggesting that the behavior of the conduction band edge is governed by the internal electron states. By contrast, the charge densities (Fig. 3) of both the B_3 and B_4 bands are mainly

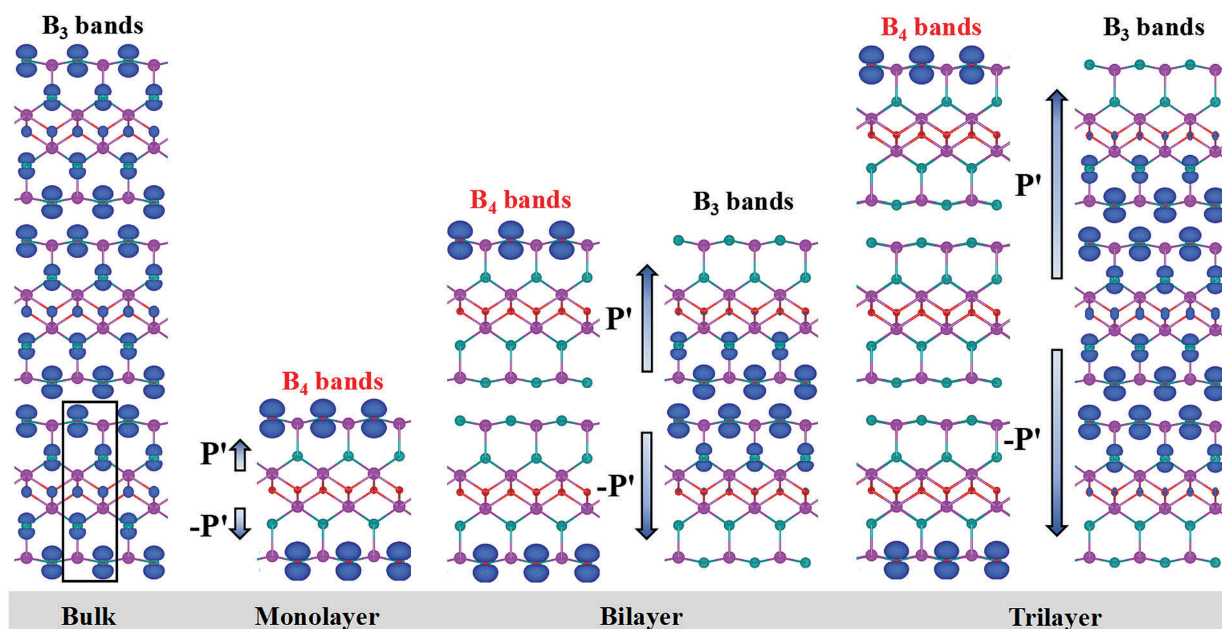

Fig. 3 Calculated band decomposed charge density of the B_3 and B_4 bands (labeled in Fig. 2a) with the isosurface value of 0.01 e $Bohr^{-3}$. Black arrows point to the direction of charge transfer from crystal internal atoms to surface atoms. P' and $-P'$ represent the two extra dipole moments induced by the charge redistribution after Bi_2OS_2 bulk being exfoliated into 2D crystals.

 This journal is © The Royal Society of Chemistry 2018

Published on 13 září 2018. Downloaded by Fail Open on 07.05.2025 10:35:25.

distributed around the sulfur atoms and look like dumbbells. Moreover, the B_4 bands entirely originate from the contribution of surface sulfur atoms, while the B_3 bands are composed of the internal sulfur electron states. This suggests that surface sulfur electron states appear when Bi_2OS_2 bulk is exfoliated into mono- and few-layers, and they greatly affect the valence band maximum (VBM) of 2D Bi_2OS_2.

Actually, these special behaviors of electron states in 2D Bi_2OS_2 can be expected by considering the significant change of interaction potential between the two separated adjacent BiS_2 layers from the bulk to the vacuum. Each Bi_2OS_2 sheet in the bulk has a triple-layer structure with a $[Bi_2O_2]^{2+}$ layer sandwiched between two $[BiS_2]^-$ layers, and thus two ionic-like local dipole moments with opposite directions from BiS_2 layer to BiO layer are produced. Because of the small vdW distance (~3.28 Å) in Bi_2OS_2, the local dipole moment from one BiS_2 layer will interact with that from the adjacent BiS_2 layer (Fig. S6, ESI†). However, when the Bi_2OS_2 bulk is exfoliated into a 2D nanosheet, the surface interaction will be broken. This induces electronic states which obviously transfer from inside the crystal to the surface, and the intrinsic SESs are thus formed. These intrinsic SESs further lead to the degeneration of surface bands (Fig. 2a), which eventually generates the anomalies in the band gap of 2D Bi_2OS_2.

The SES effect on the band gap of 2D Bi_2OS_2 can be characterized by the two extra dipole moments (Fig. 3), which are induced by the redistribution of electronic charge from inside the crystal to the surface. A dipole moment is generally defined as a product of the amount of charge at the charge center and the distance between the positive and negative charge centers. For convenience, we take the center of the spacing between the two outermost BiS_2 layers as the positive charge center and the position of the two innermost BiS_2 layers as the negative charge center. The same amount of charge transferring from inside the crystal to the outermost layers in all the 2D Bi_2OS_2 (Fig. 3) implies a linear relationship between the extra dipole moment and the distance between the two outermost layers. Furthermore, we can get a quantitative relationship between the SES effect on the band gap and the distance between the outermost layers. Moreover, Bi_2OS_2 is a vdW layered material, and the QC effect also plays an important role. Therefore, the layer-dependent band gaps (Fig. 2b) of 2D Bi_2OS_2 can be fitted to the following formula:

$$E_g\ (\text{eV}) = 0.91 + 0.42N^{-1.5} - 0.45{l_N}^{-0.1}.$$

Here the first constant term represents the band gap of the Bi_2OS_2 bulk, the second term (proportional to $N^{-1.5}$, N is the layer number) is the band gap enlarged by the QC effect, and the last (negative) term (proportional to ${l_N}^{-0.1}$, l_N is the distance between the two outermost layers) stands for the band gap reduced by the surface electron states. The band gaps enlarged by the QC effect follow the $N^{-1.5}$ power law, which decays slightly faster than that of black phosphorus ($N^{-0.73}$).[29] The reduced band gaps follow the ${l_N}^{-0.1}$ power law, which is caused by the SESs, *i.e.*, the extra dipole moments induced by the

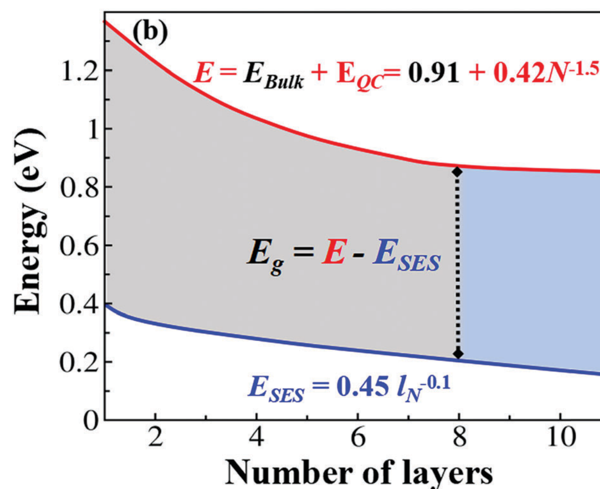

Fig. 4 Illustration of the synergistic mechanisms on the layer-dependent band gaps of 2D Bi_2OS_2 between the quantum confinement (QC) effect and the surface electron state (SES) effect. Here, N, l_N, E_{QC}, and E_{SES} stand for the number of layers, the distance between the two outermost layers, the energy gaps of 2D Bi_2OS_2 enlarged by the QC effect, and the reduced energy by the SES effect, respectively.

electron states transferring from inside the crystal to the outermost layers.[30–33] In addition, from the above formula, we can derive the band gap of the bulk limit (0.91 eV), which matches well with the calculated value (0.92 eV) and the measured optical value (0.99 eV).[19] As displayed in Fig. 4, the band gap enlarged by the QC effect follows a $0.42N^{-1.5}$ relationship, while the band gap reduced by the SESs follows a $0.45{l_N}^{-0.1}$ relationship. Clearly, both of these two effects are weakened with the increase of the stacking layers. Based on these quantitative relationships, we can obtain the minimum band gap ($E_{g(min)}$) of 0.64 eV at the 8th layer, which agrees with the DFT result (0.59 eV for 8 layers). In fact, this kind of anomaly is also likely to occur in other 2D isostructural BiS_2-based layered semiconductors (*e.g.*, $LaOBiS_2$,[34,35] $CeOBiS_2$,[36] and $SrFBiS_2$[37]).

High carrier mobility is a very desirable property for future high-speed electronic devices. The band structures of monolayer and few-layer Bi_2OS_2 near the CBM or the VBM exhibit notable dispersion behavior, suggesting that they may possess high carrier mobility. Room-temperature carrier mobilities of monolayer and few-layer Bi_2OS_2 were calculated (details are provided in Fig. S7 and S8, ESI†). As listed in Table 1, the elastic modulus of the monolayer Bi_2OS_2 is 169 J m^{-2}, two times higher than that of other Bi-related monolayers (*e.g.*, Bi_2Te_2S, ~71–75 J m^{-2}; Bi_2Te_2Se, ~64–66 J m^{-2}).[28] The in-plane electron effective mass of $m^* = 0.21m_0$ (m_0 is the free-electron mass) and the deformation potential of the electron of $|E^i| = 2.84$ eV are comparable to the values for Bi_2Te_2X (X = S, Se) and Bi_2O_2Se monolayers.[28,38] Most strikingly, an ultrahigh electron mobility of ~6.67×10^3 $cm^2\ V^{-1}\ s^{-1}$ is achieved. In addition, owing to the larger deformation potential of the hole, the hole mobility is only 490 $cm^2\ V^{-1}\ s^{-1}$, much lower than the electron mobility. This suggests that the electrons in the Bi_2OS_2 monolayer are much more mobile than the holes. For multilayer Bi_2OS_2, the

Published on 13 září 2018. Downloaded by Fail Open on 07.05.2025 10:35:25.

Table 1 Computed effective mass (m^*), 2D elastic modulus (C_{2D}), deformation potential constant ($|E^i|$), and hole and electron mobility (μ) of in-plane monolayer and few-layer Bi_2OS_2 at 300 K

Layer number	Carrier type	m^*/m_e	C_{2D} (J m^{-2})	$\|E^i\|$ (eV)	μ (10^3 cm^2 V^{-1} s^{-1})
1-Layer	Electron	0.21	169	2.84	6.67
	Hole	−0.38	169	5.85	0.49
2-Layer	Electron	0.17	352	3.52	13.9
	Hole	−0.38	352	6.96	0.72
3-Layer	Electron	0.16	524	3.33	26.6
	Hole	−0.38	524	8.50	0.73

electron mobility is almost linear with its thickness, and it can reach 26.6×10^3 cm^2 V^{-1} s^{-1} for the trilayer. In contrast, the hole mobility increases slowly with the increment of the layers, and the hole mobility of trilayer Bi_2OS_2 is only 730 cm^2 V^{-1} s^{-1}. For comparison, we also calculated the electron and hole mobility of the bulk, and their values are 28.8×10^3 cm^2 V^{-1} s^{-1} and 4.62×10^3 cm^2 V^{-1} s^{-1}, respectively (calculated details are presented in Fig. S9 and Table S1, ESI†). The large difference in the electron/hole mobility can be exploited for electron/hole separation. Detailed atomic component analysis shows that the electron transport is dominated by Bi atoms, while the hole transport is predominantly from S atoms (see Fig. S10a, ESI†). Partial charge densities near the CBM (VBM) for the monolayer and few-layer Bi_2OS_2, shown in Fig. S10b (ESI†), further reveal that the electrons (holes) come mainly from the hybridized p_x and p_y orbitals of Bi (S).

Optical properties of Bi_2OS_2 nanosheets

The moderate band gaps and large in-plane cross section suggest that Bi_2OS_2 nanosheets may exhibit a desirable in-plane light absorption across the whole solar light spectrum. Particularly, the charge densities of the conduction bands and valence bands for monolayer and few-layer Bi_2OS_2 are mainly located on different atoms (Fig. S10a, ESI†), which can effectively separate the photo-generated electron–hole pairs. The in-plane light harvesting performance of monolayer and few-layer Bi_2OS_2 is investigated.

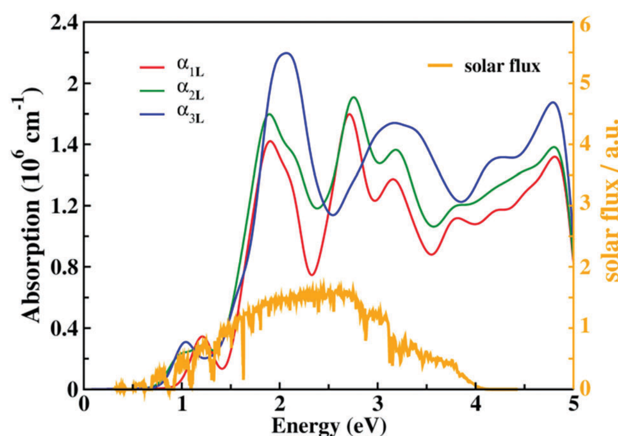

Fig. 5 Calculated absorption spectra of 2D Bi_2OS_2 with respect to the incident solar flux. α_{1L}, α_{2L} and α_{3L} represent the absorption coefficients of the monolayer, bilayer, and trilayer.

As illustrated in Fig. 5, the absorption coefficients of monolayer and few-layer Bi_2OS_2 reach to the order of 10^6 cm^{-1}, which is comparable to those of inorganic–organic hybrid perovskite solar cells.[39] Moreover, the optical absorption of monolayer and few-layer Bi_2OS_2 covers almost the entire incident solar spectrum. The trilayer even exhibits a stronger visible and UV light absorption than the monolayer and bilayer, especially in the energy range of 1.8 to 2.4 eV and 2.9 to 5.0 eV. The outstanding optical properties suggest potential applications of 2D Bi_2OS_2 for efficient optical absorber materials in solar cells or infrared detection optoelectronic devices.

Conclusions

In summary, a new 2D semiconducting Bi_2OS_2 material with a moderate band gap and ultrahigh electron mobility has been predicted. Most notably, the Bi_2OS_2 monolayer exhibits ultrahigh electron mobility up to 6.67×10^3 cm^2 V^{-1} s^{-1} while its bilayer and trilayer possess even higher electron mobilities of 13.9×10^3 cm^2 V^{-1} s^{-1} and 26.6×10^3 cm^2 V^{-1} s^{-1}, respectively. Furthermore, the band gaps of 2D Bi_2OS_2 exhibit an anomalous layer-dependent relationship that decreases from 0.97 eV to 0.57 eV, reaching the minimum value at the 8th layer and increasing afterward with the increase of stacking layers. The anomaly is a result of the synergetic effect of the QC and intrinsic SESs. In addition, monolayer and few-layer Bi_2OS_2 exhibits strong optical absorption in the whole solar spectrum region. AIMD simulation, phonon dispersion curves, and work function calculations further demonstrate the thermal, dynamic and chemical stability of the Bi_2OS_2 monolayer. The small cleavage energy (0.47 J m^{-2}) suggests feasibility of exfoliation of a monolayer from the layered bulk as well. These excellent electronic and optical properties, together with the high stability and high feasibility, endow 2D Bi_2OS_2 with great opportunities in future (opto)electronic devices.

Computational methods

All the first-principles calculations were performed using density functional theory (DFT) methods within the projected-augmented wave (PAW) potentials[40] and Perdew–Burke–Ernzerhof generalized gradient approximation (PBE-GGA)[41] as implemented in the Vienna *ab initio* simulation package (VASP).[42] The plane-wave cutoff energy was set to 500 eV. The lattice geometries and atomic positions were fully relaxed until the energy and force were converged to 10^{-5} eV and −0.01 eV Å^{-1}. A vacuum length of 15 Å was adopted to eliminate adjacent layer interactions. The PBE+D3[43,44] was employed to describe the weak interaction between layers. Phonon dispersion was calculated based on density functional perturbation theory (DFPT)[45] as embedded in the Phonopy program. *Ab initio* molecular dynamics simulations were carried out to evaluate the thermal stabilities of the Bi_2OS_2 monolayer at different temperatures. At each temperature, AIMD simulation in the

This journal is © The Royal Society of Chemistry 2018

Published on 13 září 2018. Downloaded by Fail Open on 07.05.2025 10:35:25.

NVT ensemble lasts for 5 ps with a time step of 1 fs. The temperature is controlled by using the Nose–Hoover method.[46]

Both PBE-D3 and HSE06+SOC (HSE06 plus spin–orbit coupling) were considered for band structure calculations. As shown in Fig. S11 in the ESI,† both PBE-D3 and HSE06+SOC calculations indicate that the bulk Bi_2OS_2 is a direct gap semiconductor, and the PBE-D3 band gap (0.92 eV) overall reproduces the HSE06+SOC band gap (0.80 eV) and is in good agreement with the measured optical gap (0.99 eV).[19] This indicates that PBE-D3 is an alternative for this system with affordable computational cost and is employed in this work.

The carrier mobility of few-layer Bi_2OS_2 was calculated through the formula,[47,48]

$$\mu_{2D} = \frac{e\hbar^3 C_{2D}}{k_B T m_x^* \sqrt{m_x^* m_y^*}(E^i)^2},$$

where E^i is the deformation potential constant, m_x^* (m_y^*) is the effective mass in transport direction, and C_{2D} is the 2D elastic modulus. The temperature T is set to 300 K. The E^i is derived from $\Delta E = E^i/(\Delta l/l_0)$, where ΔE is the energy shift at CBM for the electron and at VBM for the hole induced by the strain. m_x^* (m_y^*) can be estimated by $m_{x/y}^* = \hbar^2(\partial^2 E/\partial^2 k)^{-1}$, where $m_x^* = m_y^*$ due to the tetragonal lattice of few-layer Bi_2OS_2. By fitting the total energy with respect to volume change, $(E - E_0)/S_0$ to dilation $\Delta l/l_0$ with $(E - E_0)/S_0 = C_{2D}(\Delta l/l_0)^2/2$, C_{2D} along the transport direction can be determined.

The optical absorption coefficient $\alpha(\omega)$ was calculated from the following relation[49]

$$\alpha(\omega) = \sqrt{2}\frac{\omega}{c}\left[\sqrt{\varepsilon_1^2(\omega) + \varepsilon_2^2(\omega)} - \varepsilon_1(\omega)\right]^{1/2},$$

where $\varepsilon_1(\omega)$ is the real part of dielectric function, and $\varepsilon_2(\omega)$ is the imaginary part of dielectric function.

Conflicts of interest

The authors declare no competing financial interests.

Acknowledgements

This work is supported by the National Key Research and Development Program of China (2017YFA0204800), National Natural Science Foundation of China (21525311, 21773027, 51435003, 21803032), Jiangsu 333 project (BRA2016353), the Scientific Research Foundation of Graduate School of Southeast University (YBJJ1773), and the Fundamental Research Funds for the Central Universities of China. The authors are thankful for the computational resources at the SEU and National Supercomputing Center in Tianjin.

Notes and references

1 Y. Ma, A. Kuc, J. Yu, P. Philipsen and T. Heine, *Angew. Chem., Int. Ed.*, 2017, **56**, 1–6.
2 Y. Zhang, T. R. Chang, B. Zhou, Y. T. Cui, H. Yan, Z. K. Liu, F. Schmitt, J. Lee, R. Moore and Y. L. Chen, *Nat. Nanotechnol.*, 2014, **9**, 111–115.
3 C. Zhang and S. Qiang, *J. Phys. Chem. Lett.*, 2016, **7**, 2664–2670.
4 Y. Pan, L. Zhang, L. Huang, L. Li, L. Meng, M. Gao, Q. Huan, X. Lin, Y. Wang and S. Du, *Small*, 2014, **10**, 2215–2225.
5 J. Lu, A. Carvalho, X. K. Chan, H. Liu, B. Liu, E. S. Tok, K. P. Loh, A. H. Castro Neto and C. H. Sow, *Nano Lett.*, 2015, **15**, 3524–3532.
6 B. Radisavljevic and A. Kis, *Nat. Nanotechnol.*, 2013, **8**, 147–148.
7 J. O. Island, G. A. Steele, D. Z. Van, S. J. Herre and A. Castellanos-Gomez, *2D Mater.*, 2014, **2**, 011002.
8 A. Ziletti, A. Carvalho, D. K. Campbell, D. F. Coker and A. H. Castro Neto, Oxygen defects in phosphorene, *Phys. Rev. Lett.*, 2014, **114**, 046801.
9 H. Cheng, B. Huang and Y. Dai, *Nanoscale*, 2014, **6**, 2009–2026.
10 Y. Pu, T. Liu, Y. Huang, C. Chen, I. K. Sun and H. J. Seo, *J. Nanopart. Res.*, 2015, **17**, 1–11.
11 L. Zhang, W. Wang, L. Zhou and H. Xu, *Small*, 2010, **3**, 1618–1625.
12 G. Chen, Y. Yu, K. Zheng, T. Ding, W. Wang, Y. Jiang and Q. Yang, *Small*, 2015, **11**, 2848–2855.
13 X. Meng and Z. Zhang, *J. Mol. Catal. A: Chem.*, 2016, **423**, 533–549.
14 X. Meng and Z. Zhang, *J. Photoch. Photobio. A*, 2015, **310**, 33–44.
15 Y. Bai, L. Ye, L. Wang, X. Shi, P. Wang and W. Bai, *Environ. Sci.: Nano*, 2016, **3**, 902–909.
16 X. J. Wen, C. G. Niu, L. Zhang and G. M. Zeng, *Dalton Trans.*, 2017, **46**, 486–493.
17 H. Zhang, J. Huang, X. Zhou and X. Zhong, *Inorg. Chem.*, 2011, **50**, 7729–7734.
18 G. L. Fang, G. Chen, X. Wang and J. Q. Liu, *Sci. China: Technol. Sci.*, 2011, **54**, 19–22.
19 A. Miura, Y. Mizuguchi, T. Takei, N. Kumada, E. Magome, C. Moriyoshi, Y. Kuroiwa and K. Tadanaga, *Solid State Commun.*, 2016, **227**, 19–22.
20 V. Nicolosi, M. Chhowalla, M. G. Kanatzidis, M. S. Strano and J. N. Coleman, *Science*, 2013, **340**, 1420–1438.
21 J. N. Coleman and V. Nicolosi, *Science*, 2011, **42**, 568–571.
22 R. Zacharia, H. Ulbricht and T. Hertel, *Phys. Rev. B: Condens. Matter Mater. Phys.*, 2003, **69**, 155406.
23 J. H. Zhang, F. Z. Ren, M. S. Deng and Y. X. Wang, *Phys. Chem. Chem. Phys.*, 2015, **17**, 10218–10226.
24 J. Yu, Y. Ma, Y. Li and T. Heine, *Nano Lett.*, 2017, **17**, 1833–1838.
25 S. Zhang, S. Guo, Z. Chen, Y. Wang, H. Gao, J. Gomez-Herrero, P. Ares, F. Zamora, Z. Zhu and H. Zeng, *Chem. Soc. Rev.*, 2018, **47**, 982–1021.
26 H. S. Lee, S. W. Min, Y. G. Chang, M. K. Park, T. Nam, H. Kim, J. H. Kim, S. Ryu and S. Im, *Nano Lett.*, 2012, **12**, 3695–3700.
27 W. S. Yun, S. W. Han, S. C. Hong, I. G. Kim and J. D. Lee, *Phys. Rev. B: Condens. Matter Mater. Phys.*, 2012, **85**, 033305.
28 B. Wang, X. H. Niu, Y. X. Ouyang, Q. H. Zhou and J. L. Wang, *J. Phys. Chem. Lett.*, 2018, **9**, 487–490.
29 V. Tran, R. Soklaski, Y. F. Liang and L. Yang, *Phys. Rev. B: Condens. Matter Mater. Phys.*, 2014, **89**, 235319.

30 Q. H. Zhou, Q. Li, S. J. Yuan, Q. Chen and J. L. Wang, *Phys. Chem. Chem. Phys.*, 2017, **19**, 29232–29236.
31 A. Singh, R. D. Gunning, A. Sanyal and K. M. Ryan, *Chem. Commun.*, 2010, **46**, 7193–7195.
32 J. Pan, Z. Wang, Q. Chen, J. Hu and J. Wang, *Nanoscale*, 2014, **6**, 13565–13571.
33 S. Yang, D. Prendergast and J. B. Neaton, *Nano Lett.*, 2012, **12**, 383–388.
34 R. Sagayama, H. Sagayama, R. Kumai, Y. Murakami, T. Asano, J. Kajitani, R. Higashinaka, T. D. Matsuda and Y. Aoki, *J. Phys. Soc. Jpn.*, 2015, **84**, 123703.
35 J. J. Pulikkotil and S. Auluck, *J. Alloys Compd.*, 2015, **626**, 208–211.
36 R. Higashinaka, T. Asano, T. Nakashima, K. Fushiya, Y. Mizuguchi, O. Miura, T. D. Matsuda and Y. Aoki, *J. Phys. Soc. Jpn.*, 2015, **84**, 023702.
37 H. Lei., K. Wang, M. Abeykoon, E. S. Bozin and C. Petrovic, *Inorg. Chem.*, 2013, **52**, 10685–10689.
38 J. X. Wu, H. T. Yuan, M. M. Meng, C. Chen, Y. Sun, Z. Y. Chen, W. H. Dang, C. W. Tan, Y. J. Liu, J. B. Yin, Y. B. Zhou, S. Y. Huang, H. Q. Xu, Y. Cui, H. Y. Hwang, Z. F. Liu, Y. L. Chen, B. H. Yan and H. L. Peng, *Nat. Nanotechnol.*, 2017, **12**, 530–534.
39 N. J. Jeon, J. H. Noh, Y. C. Kim, W. S. Yang, S. Ryu and S. I. Seok, *Nat. Mater.*, 2014, **13**, 897–903.
40 P. E. Blöchl, *Phys. Rev. B: Condens. Matter Mater. Phys.*, 1994, **50**, 17953.
41 J. P. Perdew, K. Burke and M. Ernzerhof, *Phys. Rev. Lett.*, 1996, **77**, 3865.
42 G. Kresse and J. Furthmuller, *Phys. Rev. B: Condens. Matter Mater. Phys.*, 1996, **54**, 11169.
43 S. Grimme, J. Antony, S. Ehrlich and H. Krieg, *J. Chem. Phys.*, 2010, **132**, 154104.
44 S. Grimme, S. Ehrlich and L. Goerigk, *J. Comput. Chem.*, 2011, **32**, 1456–1465.
45 X. Gonze, *Phys. Rev. B: Condens. Matter Mater. Phys.*, 1997, **55**, 10355.
46 G. J. Martyna, M. L. Klein and M. Tuckerman, *J. Chem. Phys.*, 1992, **97**, 2635.
47 J. Qiao, X. Kong, Z. X. Hu, F. Yang and W. Ji, *Nat. Commun.*, 2014, **5**, 4475.
48 Q. S. Wu, W. W. Xu, B. Y. Qu, L. Ma, X. H. Niu, J. L. Wang and X. C. Zeng, *Mater. Horiz.*, 2017, **4**, 1085–1091.
49 S. Lalitha, S. Z. Karazhanov, P. Ravindran, S. Senthilarasu, R. Sathyamoorthy and J. Janabergenov, *Phys. Rev. B: Condens. Matter Mater. Phys.*, 2007, **387**, 227–238.

Published on 13 zái 2018. Downloaded by Fail Open on 07.05.2025 10:35:25.

This journal is © The Royal Society of Chemistry 2018